

A transition from boundary- to bulk-driven acoustic streaming due to nonlinear thermoviscous effects at high acoustic energy densities

Jonas Helboe Joergensen,^{1,*} Wei Qiu,^{2,†} and Henrik Bruus^{1,‡}

¹*Department of Physics, Technical University of Denmark,
DTU Physics Building 309, DK-2800 Kongens Lyngby, Denmark*

²*Department of Biomedical Engineering, Lund University, Ole Römers väg 3, 22363, Lund, Sweden*

(Dated: 21 December 2021)

Acoustic streaming is studied in a rectangular microfluidic channel. It is demonstrated theoretically, numerically, and experimentally with good agreement, frictional heating can alter the streaming pattern qualitatively at high acoustic energy densities E_{ac} above 500 J/m^3 . The study shows, how as a function of increasing E_{ac} at fixed frequency, the traditional boundary-driven four streaming rolls created at a half-wave standing-wave resonance, transition into two large streaming rolls. This nonlinear transition occurs because friction heats up the fluid resulting in a temperature gradient, which spawns an acoustic body force in the bulk that drives thermoacoustic streaming.

Microscale acoustofluidic devices are used to manipulate and control microparticles and cells. In such devices, two main forces act on the suspended particles, the acoustic radiation force and the drag force due to acoustic streaming, which is a time-averaged flow caused by the inherent nonlinearities of fluid dynamics. Recent work has clarified many subtle details pertaining to the radiation force on microparticles, including thermoviscous effects [1] and microstreaming [2]. Concurrently, similar progress has been made in the theory of acoustic streaming, especially regarding thermoviscous effects. The fundamental boundary-driven streaming caused by time-averaged forces in the oscillatory boundary-layer flow [3], and the fundamental bulk-driven streaming generated by the time-averaged dissipation of traveling waves [4], have recently been supplemented by bulk-driven baroclinic [5, 6] and thermoacoustic [7, 8] streaming, caused by an interplay between standing acoustic waves and steady temperature gradients. However, as noted in Refs. [7, 8], the validity of the conventional perturbation approach breaks down at moderately high, but experimentally obtainable acoustic energy densities above 100 J/m^3 in combination with moderate thermal gradients above 1 K/mm . This need for an extension of the theory beyond perturbation theory is addressed in this Letter and in the accompanying detailed presentation of the nonperturbative model in Ref. [9].

We introduce a nonperturbative iteration approach to investigate theoretically and numerically, the nonlinear effects appearing in a conventional acoustofluidic channel at high acoustic energy density E_{ac} , and we validate experimentally the model predictions. We take as our generic acoustofluidic model system, the widely used rectangular channel driven at resonance with a transverse half-wave standing acoustic wave, for which the streaming at low E_{ac} is dominated by conventional boundary-driven streaming with four streaming rolls [10–13]. We show how nonlinear effects in the form of heating by viscous dissipation from the acoustic field inside the bound-

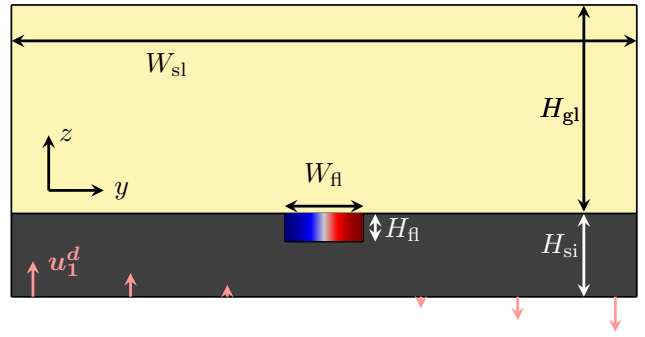


FIG. 1. Cross-section of the modeled rectangular channel of width $W_{fl} = 375 \mu\text{m}$ and height $H_{fl} = 135 \mu\text{m}$ embedded in a silicon base of width $W_{sl} = 3 \text{ mm}$ and height $H_{si} = 0.4 \text{ mm}$, and covered by a glass lid of height $H_{gl} = 1 \text{ mm}$. The bottom-edge actuation is the displacement $\mathbf{u}_1^d = d_0(y/W_{sl}) \mathbf{e}_y$ with an adjustable amplitude d_0 at frequency $f_0 = 1.911 \text{ MHz}$.

ary layers, set up a steady temperature gradient. This gradient drives a strong thermoacoustic streaming in the bulk, which changes the streaming flow qualitatively from four to two flow rolls, and which by thermal convection alters the temperature field. Our analysis of this nonlinear phenomenon and its underlying mechanism fills a knowledge gap in nonlinear acoustics, and it provides a guidance for understanding and optimizing acoustofluidic systems running at high E_{ac} such as high-intensity ultrasound focusing [14–16], acoustic streaming-based micromixers [17–20], particle manipulation devices [21–23], and high-throughput acoustophoresis devices [24–26].

Physical model.—We consider a long straight microchannel with a cross-sectional of width $W_{fl} = 375 \mu\text{m}$ and height $H_{fl} = 135 \mu\text{m}$ embedded in a silicon base with a glass lid, see Fig. 1 and Refs. [9–13]. To excite the horizontal half-wave resonance mode in the fluid, the system is actuated at frequency $f_0 = 1.911 \text{ MHz}$ by the bottom-edge displacement sketched in Fig. 1. The response to the acoustic actuation is governed by the conservation

equation for mass, momentum, and energy in the fluid and solid. The independent fields are the pressure p , the velocity \mathbf{v} , and the temperature T in the fluid, and the displacement \mathbf{u} and T in the solid.

We study a fluid characterized by the following material parameters: density ρ , isothermal compressibility κ_T , thermal conductivity k^{th} , specific heat c_p , dynamic and bulk viscosity η and η^{b} , thermal expansion coefficient α_p , the ratio of specific heats $\gamma = c_p/c_v$, and the isentropic and isothermal compressibility κ_s and $\kappa_T = \gamma\kappa_s$. The temperature dependence of the parameters for water are given by the polynomials derived in Ref. [12]. The elastic solid is characterized by density ρ , longitudinal and transverse sound speed c_{lo} and c_{tr} , thermal conductivity k^{th} , thermal expansion coefficient α_{p0} and isothermal compressibility κ_T [9].

We use the iterative thermoviscous model presented in our concurrent paper [9], a model that is nonperturbative unlike the perturbative models traditionally used in acoustofluidics [7, 12]. The model exploits that the acoustic fields varies much faster ($\sim 10^{-7}$ s) than the hydrodynamic and thermal flows ($\sim 10^{-2}$ s), so that the fast and slow dynamics can be solved separately. Here, we study the stationary limit of the slow time scale and describe any given physical field Q_{phys} as a sum of a stationary field Q_0 and a time-varying acoustic field $\text{Re}\{Q_1 e^{-i\omega t}\}$ with a stationary complex-valued amplitude Q_1 ,

$$Q_{\text{phys}}(t) = Q_0 + \text{Re}\{Q_1 e^{-i\omega t}\}. \quad (1)$$

A product of two acoustic fields will contain a steady part $\langle a_1 b_1 \rangle = \frac{1}{2} \text{Re}\{a_1 b_1^*\}$ where the asterisk denotes complex conjugation. We neglect higher harmonics with angular frequency $n\omega$, $n = 2, 3, \dots$. In Ref. [9], we use this ansatz to separate the governing equations in a set that controls the acoustic fields, and a set that controls the stationary fields.

Acoustofluidic systems also exhibit dynamics on two different length scales, one set by the wavelength of the acoustic fields and one set by the viscous and thermal boundary layers. The boundary conditions on the velocity field, stress, heat flux, and temperature at the fluid-solid interface results in the appearance of thermal boundary layer of width δ_t in both the fluid and the solid, and in a viscous boundary layer of width δ_s in the fluid. These boundary layers are localized near fluid-solid interfaces, and their dynamically-defined widths (jointly called δ) are small compared to a typical device size or wavelength d [1], $\delta_s = \sqrt{2\nu_0/\omega}$ and $\delta_t \approx \sqrt{2D^{\text{th}}/\omega}$. Typically, $\delta_t \lesssim \delta_s \lesssim 500$ nm, which is more than two orders of magnitude smaller than $d \sim 100$ μm . In our model [9], we use $\delta \ll d$ to separate the fields into a bulk field (d) and boundary layer field (δ), that are connected through the boundary conditions at the fluid-solid interface. The model presented in Ref. [9] uses the separation of time and length scales to setup an iterative model with ef-

fective boundary conditions that enables simulations of nonperturbative acoustofluidic systems without numerically resolving the viscous and thermal boundary layers. All dependent fields are given analytically by the independent fields as shown in Ref. [9].

Acoustic fields.—In the thermoviscous model of Ref. [9], the acoustics is fully described by the pressure field p_1 in the fluid and by the displacement field \mathbf{u}_1^d in the solid through the Helmholtz and Cauchy equations,

$$\nabla^2 p_1 = -k_c^2 p_1, \quad k_c = \frac{\omega}{c_0} (1 + i\Gamma_{0c}^{\text{fl}}), \quad (2a)$$

$$-\rho\omega^2 \mathbf{u}_1^d = \nabla \cdot \boldsymbol{\sigma}_1^{d,\text{sl}}, \quad (2b)$$

$$\begin{aligned} \boldsymbol{\sigma}_1^{d,\text{sl}} = & -\frac{\alpha_p}{\kappa_T} T_1 \mathbf{I} + \rho c_{\text{tr}}^2 \left[\nabla \mathbf{u}_1 + (\nabla \mathbf{u}_1)^T \right] \\ & + \rho (c_{\text{lo}}^2 - 2c_{\text{tr}}^2) (\nabla \cdot \mathbf{u}_1) \mathbf{I}, \end{aligned} \quad (2c)$$

where $\boldsymbol{\sigma}_1$ is the stress tensor. p_1 and \mathbf{u}_1^d are connected through effective boundary conditions on the fluid-solid interface taking the boundary layers into account analytically: a no-slip condition for the velocity and a continuity condition on the stress, as described in Ref. [9]. The acoustic velocity \mathbf{v}_1 and the temperature field T_1 are given by p_1 and the analytical boundary-layer fields [7].

Stationary fields.—The stationary fields are the pressure p_0 and streaming velocity \mathbf{v}_0^d in the fluid, and the temperature T_0^d in the solid and fluid. The acoustic timescale affects T_0^d , p_0 , and \mathbf{v}_0^d through bulk terms (heating and the acoustic body force \mathbf{f}_{ac}^d) and corrections due to the boundary layers to the boundary conditions. The governing equations for \mathbf{v}_0^d and p_0 are [9],

$$0 = \nabla \cdot \mathbf{v}_0^d, \quad (3a)$$

$$0 = -\nabla \left[p_0^d - \langle \mathcal{L}_{\text{ac}}^d \rangle \right] + \eta_0 \nabla^2 \mathbf{v}_0^d - \nabla \cdot \left[\rho_0 \mathbf{v}_0 \mathbf{v}_0 \right] + \mathbf{f}_{\text{ac}}^d. \quad (3b)$$

$$\begin{aligned} \mathbf{f}_{\text{ac}}^d = & -\frac{1}{4} |\mathbf{v}_1^{d,p}|^2 \nabla \rho_0 - \frac{1}{4} |p_1|^2 \nabla \kappa_s \\ & + \left(1 - \frac{2a_\eta(\gamma-1)}{\beta+1} \right) \frac{\Gamma\omega}{c_0^2} \langle \mathbf{v}_1^{d,p} p_1 \rangle \\ & + 2a_\eta \eta_0 (\gamma-1) \frac{\omega}{c_0^2} \langle i\mathbf{v}_1^{d,p} \cdot \nabla \mathbf{v}_1^{d,p} \rangle. \end{aligned} \quad (3c)$$

The boundary layers generate a slip velocity on the solid-fluid interface, and the resulting effective boundary condition on \mathbf{v}_0^d is [9],

$$\mathbf{v}_0^{d0} = (\mathbf{A} \cdot \mathbf{e}_x) \mathbf{e}_x + (\mathbf{A} \cdot \mathbf{e}_y) \mathbf{e}_y + (\mathbf{B} \cdot \mathbf{e}_z) \mathbf{e}_z, \quad (4a)$$

$$\begin{aligned} \mathbf{A} = & -\frac{1}{2\omega} \text{Re} \left\{ \mathbf{v}_1^{\delta 0*} \cdot \nabla \left(\frac{1}{2} \mathbf{v}_1^{\delta 0} - i\mathbf{V}_1^{00} \right) - i\mathbf{V}_1^{00*} \cdot \nabla \mathbf{v}_1^{d,p} \right. \\ & \left. + \left[\frac{2-i}{2} \nabla \cdot \mathbf{v}_1^{\delta 0*} + i \left(\nabla \cdot \mathbf{V}_1^{00*} - \partial_z v_{1z}^{d*} \right) \right] \mathbf{v}_1^{\delta 0} \right\} \\ & + \frac{1}{2\eta_0} \text{Re} \left\{ \eta_1^{d0} \mathbf{v}_1^{\delta 0*} + \frac{1}{1 - i\delta_s/\delta_t} \eta_1^{\delta 0} \mathbf{v}_1^{\delta 0*} \right\}, \end{aligned} \quad (4b)$$

$$\mathbf{B} = \frac{1}{2\omega} \text{Re} \left\{ i \mathbf{v}_1^{d0*} \cdot \nabla \mathbf{v}_1^{d,p} \right\}. \quad (4c)$$

Here, \mathbf{V}_1^0 is the velocity of the fluid-solid interface, \mathbf{e}_z is the surface normal vector, and \mathbf{e}_x and \mathbf{e}_y are perpendicular to \mathbf{e}_z . The streaming flow \mathbf{v}_0^d can be driven either by the acoustic body force \mathbf{f}_{ac}^d , called bulk-driven streaming, or by the effective boundary condition on \mathbf{v}_0^{d0} , called boundary-driven streaming.

The stationary temperature $T_0^{d,fl}$ in the fluid is governed by the heat equation (energy conservation) [9],

$$0 = -\nabla \cdot \left[k_0^{\text{th}} \nabla T_0^{\text{fl},d} \right] - c_p \rho_0 \mathbf{v}_0 \cdot \nabla T_0^{\text{fl},d} + P_{ac}^d, \quad (5a)$$

$$P_{ac}^d = -\nabla \cdot \left[\langle k_1^{\text{th},d} \nabla T_1^d \rangle - \langle p_1 \mathbf{v}_1^{d,p} \rangle + \langle \mathbf{v}_1^{d,p} \cdot \boldsymbol{\tau}_1^d \rangle \right] - c_p \langle \rho_1^d \mathbf{v}_1^{d,p} \rangle \cdot \nabla T_0^d, \quad (5b)$$

and similarly for $T_0^{d,sl}$ in the solid [9],

$$0 = -\nabla \cdot \left[k_0^{\text{th}} \nabla T_0^{\text{sl},d} \right] + P_{ac}^d \quad (6a)$$

$$P_{ac}^d = -\nabla \cdot \langle k_1^{\text{th},sl} \nabla T_1^{\text{sl},d} \rangle \quad (6b)$$

Here, P_{ac}^d is the power density delivered by the acoustic wave through frictional dissipation and energy flux. $T_0^{d,fl}$ and $T_0^{d,sl}$ are connected at the fluid-solid interface by the two effective boundary conditions taking the boundary layers into account analytically: continuity of temperature and of heat flux, applied respectively as a Dirichlet condition on $T_0^{d,fl}$ and a flux condition on $\mathbf{n} \cdot \nabla T_0^{d,sl}$ [9],

$$T_0^{\text{fl},d} = T_0^{\text{sl},d} - T_0^{\text{fl},\delta 0} - \frac{1}{2} \text{Re} \left\{ \mathbf{u}_1 \cdot \nabla T_1^{\text{fl},d*} - k_t^{\text{fl}} (\mathbf{u}_1 \cdot \mathbf{n}) T_1^{\text{fl},\delta 0*} \right\}, \quad (7a)$$

$$k_0^{\text{th},sl} \mathbf{n} \cdot \nabla T_0^{\text{sl},d} = k_0^{\text{th},fl} \mathbf{n} \cdot \nabla T_0^{\text{fl},d} + k_0^{\text{th},fl} \partial_z T_0^{\text{fl},\delta} + \frac{1}{2} \text{Re} \left\{ k_t^{\text{fl}} k_1^{\text{th},fl} T_1^{\text{fl},\delta*} - \frac{2i}{\delta_t^2} k_0^{\text{th},fl} (\mathbf{u}_1 \cdot \mathbf{n}) T_1^{\text{fl},\delta*} \right\} \quad (7b)$$

In summary, the bulk temperature T_0^d is governed by the heat equations (5) and (6) together with the effective boundary conditions (7).

Experimental method.—The experiments were performed using a long straight microchannel of width $W = 375 \mu\text{m}$ and height $H = 135 \mu\text{m}$ in a glass-silicon chip with a piezoelectric transducer glued underneath. The transducer was driven at a frequency of 1.97 MHz at input power $P_{in} = 6.1, 86.8, \text{ and } 182.5 \text{ mW}$, resulting in the energy density $E_{ac} = 27.2 \pm 1.1, 388.7 \pm 15.9, \text{ and } 817.3 \pm 33.5 \text{ J/m}^3$, respectively, as measured from the focusing of 5.0- μm -diameter particles at 140 fps using confocal micro-particle image velocimetry (μPIV) at the low P_{in} [27]. At higher P_{in} , E_{ac} is estimated using the proportionality $E_{ac} \propto P_{in}$. The confocal μPIV technique only captures the particle motion near the focal plane (channel mid-height), excluding particles near

the top and bottom walls influenced by hydrodynamic and acoustic particle-wall interactions, and as a result, E_{ac} is measured accurately. The acoustic streaming for each E_{ac} was measured at 10 to 60 fps by tracking the motion of 0.5- μm -diameter particles using a defocusing-based 3D particle tracking technique [28–30]. To avoid the resonance frequency shift due to the temperature rise of the transducer under moderate (86.8 mW) and high (182.5 mW) P_{in} , each measurement was run for 2 s and repeated 100 times to improve the statistics, resulting in 7800–12000 recorded frames for each driving condition.

Results and discussion.—The simulation and experimental results shown in Fig. 2 reveal the dominant nonlinear behavior of the stationary streaming \mathbf{v}_0^d and temperature T_0 in a standard acoustofluidic device. In the linear regime at low $E_{ac} \lesssim 30 \text{ J/m}^3$, \mathbf{v}_0^d is dominated by the boundary-driven streaming entering the model through the slip-velocity condition (4), and the usual four boundary-driven streaming rolls appear, see Fig. 2(a). Due to friction in the viscous boundary layers, heat is generated both at the top and bottom of the channel. At the bottom, this heat is removed efficiently because of the high heat conductivity of silicon. At the top, however, the heat is removed less efficiently by the lower heat conductivity of glass, and a steady temperature gradient ∇T_0 is established, which explains the temperature T_0^d seen in Fig. 2(f).

The gradient ∇T_0 created by the acoustic frictional heating results in gradients in $\nabla \rho_0$ and $\nabla \kappa_0$, thus inducing a thermoacoustic body force (3c) \mathbf{f}_{ac}^d [7, 8],

$$\begin{aligned} \mathbf{f}_{ac}^d &\approx -\frac{1}{4} |p_1|^2 \nabla \kappa_{s,0} - \frac{1}{4} |\mathbf{v}_1|^2 \nabla \rho_0 \\ &= -\frac{1}{4} |p_1|^2 \left(\frac{\partial \kappa_s}{\partial T} \right)_{T_0} \nabla T_0 - \frac{1}{4} |\mathbf{v}_1|^2 \left(\frac{\partial \rho}{\partial T} \right)_{T_0} \nabla T_0. \end{aligned} \quad (8)$$

Since $|p_1|^2 \propto |\mathbf{v}_1|^2 \propto E_{ac}$ and $|\nabla T_0| \propto P_{ac}^d \propto E_{ac}$, we have $|\mathbf{f}_{ac}^d| \propto E_{ac}^2$, and \mathbf{f}_{ac}^d will become important in the bulk at high E_{ac} and cause qualitative nonlinear changes of the streaming pattern. According to Eq. (8), \mathbf{f}_{ac}^d is pointing toward high temperature at the top and is strongest at the pressure antinodes at the sides [7, 8]. Consequently, \mathbf{f}_{ac}^d pushes liquid from the sides up toward the top center, with a back-flow down along vertical center axis, thus creating a streaming pattern that consists of two streaming rolls in each side of the channel. This pattern is seen at the high $E_{ac} = 5300 \text{ J/m}^3$ in Fig. 2(d), where the streaming is completely dominated by the thermoacoustic streaming. The transition from boundary-driven streaming at low E_{ac} to bulk-driven streaming at high E_{ac} is studied qualitatively in Fig. 2(a)–(d) and quantitatively in Fig. 2(e). During the transition, the two bottom streaming rolls expand and the two top rolls shrink, see Fig. 2(b)–(c) at $E_{ac} = 380$ and 800 J/m^3 , respectively. The bottom rolls expand because they rotate the same way as the two thermoacoustic streaming rolls.

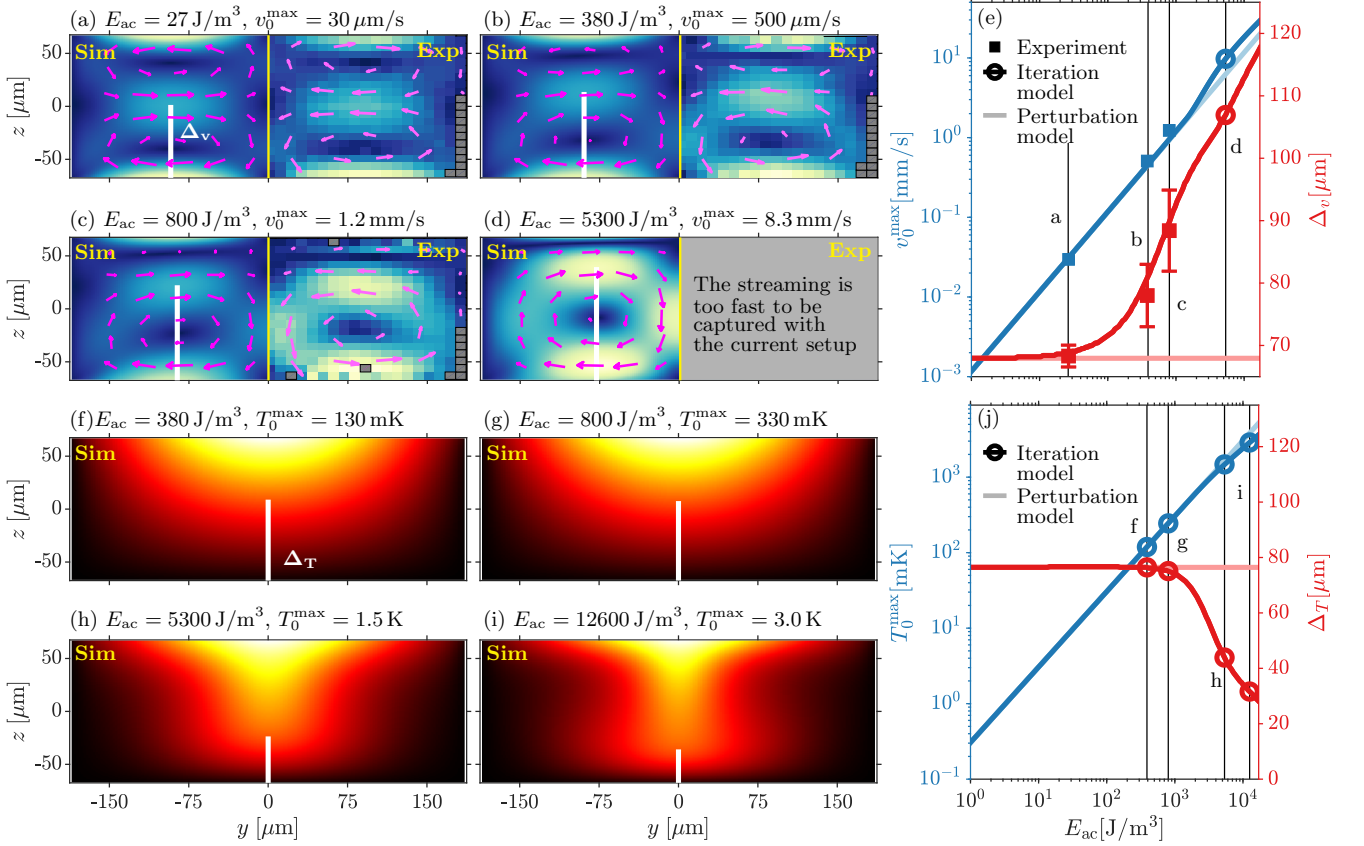


FIG. 2. Simulation and experimental results for \mathbf{v}_0 and T_0 in the microchannel. (a)-(d) Vector of \mathbf{v}_0 and color plot of $|\mathbf{v}_0|$ from 0 (blue) to v_0^{\max} (yellow) at four E_{ac} . For each E_{ac} , the left half are simulations and the right half are experiments. Δ_v (white bar) is the height where v_{0y} is maximal. (e) Plots of v_0^{\max} and Δ_v vs. E_{ac} with data from simulations and experiments, showing the transition from boundary- to bulk-driven streaming. The error bars on experimental v_0^{\max} and E_{ac} are within the square markers. The round markers represent the simulations shown in panels (d) and (f)-(i). (f)-(i) Color plot of simulated temperature increase T_0 from 0 (black) to T_0^{\max} at four E_{ac} . Δ_T (white bar) is the height where $T_0 = \frac{1}{2}T_0^{\max}$. (j) Plots of simulated T_0^{\max} and Δ_T vs. E_{ac} showing a transition from diffusion- to convection-dominated heat transport.

This transition is studied quantitatively in Fig. 2(e) by plotting the maximum streaming velocity v_0^{\max} and the vertical distance Δ_v (thick white line) from the bottom of the channel to the position of the maximum horizontal streaming velocity $\max(v_{0y})$ toward the center occurs. In the log-log plot (dark blue), the perturbative result $v_0^{\max} \propto E_{ac}$ is valid up to $E_{ac} \approx 1000 J/m^3$, but at higher values v_0^{\max} increases faster. A stronger signal is seen in the log-lin plot (dark red), where the perturbative result $\Delta_v \propto E_{ac}^0$ only holds for $E_{ac} \lesssim 30 J/m^3$, after which point Δ_v increases with increasing E_{ac} .

As the streaming velocity increases, convection becomes increasingly important for the heat transport (5) and strongly affects the temperature field, see Fig. 2(f-i) for $E_{ac} = 380, 800, 5300,$ and $12,600 J/m^3$. Convection becomes important at a Péclet number $Pe = |\mathbf{v}_0|H_{fl}/D^{th} \sim 1$ corresponding to $|\mathbf{v}_0| \sim 1$ mm/s, consistent with Fig. 2(f-j). Qualitatively, we see that for

$E_{ac} \gtrsim 800 J/m^3$, the two flow rolls pull the temperature profile down along the vertical center axis. We quantify this effect by the maximum temperature T_0^{\max} and the vertical distance Δ_T along the center axis from the bottom edge to the point where $T_0 = \frac{1}{2}T_0^{\max}$. The thermoacoustic streaming increases the heat transport from the fluid-glass interface to the silicon wafer, thus T_0^{\max} increases less steeply than the perturbative result, $T_0^{\max} \propto E_{ac}$, as seen in the log-log plot (blue) of T_0^{\max} vs. E_{ac} for $E_{ac} \gtrsim 5000 J/m^3$ in Fig. 2(j). A stronger signal is seen in the log-lin plot (dark red), where the perturbative result $\Delta_T \propto E_{ac}^0$ only holds for $E_{ac} \lesssim 500 J/m^3$, after which point Δ_T decreases with increasing E_{ac} .

Conclusion.—In this Letter we have shown numerically and experimentally that the acoustic streaming in a standard microscale acoustofluidic device is changed qualitatively for moderately high acoustic energy densities $E_{ac} \gtrsim 500 J/m^3$. We have explained this effect

by a nonperturbative model [9], in which a transition from boundary- to bulk-driven acoustic streaming occurs, as the acoustic body force \mathbf{f}_{ac} begins to dominate the streaming at increased E_{ac} due to the internal heating generated in the viscous boundary layers. We have shown good qualitative and quantitative agreement between our model predictions and experimental data.

$E_{ac} \gtrsim 500 \text{ J/m}^3$ can easily be obtained in standard acoustofluidic devices, where $E_{ac} \approx 10 - 50 \text{ J/m}^3 \times [U_{pp}/(1 \text{ V})]^2$ has been reported in the literature, U_{pp} being the applied voltage on the piezoelectric transducer [11, 31–33]. The physical understanding of how such acoustofluidic devices behave at high E_{ac} is important for the continued development of high throughput devices in particular for biotech applications.

We thank R. Barnkob and M. Rossi for providing the software DefocusTracker, defocustracking.com/. WQ was supported by MSCA EF Seal of Excellence IF-2018 from Vinnova, Sweden’s Innovation Agency (Grant No. 2019-04856). HB and JHJ was supported by Independent Research Fund Denmark, Natural Sciences (Grant No. 8021-00310B).

* jonashj@fysik.dtu.dk

† wei.qiu@bme.lth.se

‡ bruus@fysik.dtu.dk

- [1] J. T. Karlsen and H. Bruus, Forces acting on a small particle in an acoustical field in a thermoviscous fluid, *Phys. Rev. E* **92**, 043010 (2015).
- [2] T. Baasch, A. Pavlic, and J. Dual, Acoustic radiation force acting on a heavy particle in a standing wave can be dominated by the acoustic microstreaming, *Phys. Rev. E* **100**, 061102 (2019).
- [3] Lord Rayleigh, On the circulation of air observed in Kundt’s tubes, and on some allied acoustical problems, *Philos. Trans. R. Soc. London* **175**, 1 (1884).
- [4] C. Eckart, Vortices and streams caused by sound waves, *Phys. Rev.* **73**, 68 (1948).
- [5] G. Chini, Z. Malecha, and T. Dreeben, Large-amplitude acoustic streaming, *J. Fluid Mech.* **744**, 329 (2014).
- [6] G. Michel and C. Gissinger, Cooling by baroclinic acoustic streaming, *Phys. Rev. Applied* **16**, L051003 (2021).
- [7] J. H. Joergensen and H. Bruus, Theory of pressure acoustics with thermoviscous boundary layers and streaming in elastic cavities, *J. Acoust. Soc. Am.* **149**, 3599 (2021).
- [8] W. Qiu, J. H. Joergensen, E. Corato, H. Bruus, and P. Augustsson, Fast microscale acoustic streaming driven by a temperature-gradient-induced non-dissipative acoustic body force, *Phys. Rev. Lett.* **127**, 064501 1 (2021).
- [9] J. H. Joergensen and H. Bruus, Theory and modeling of nonperturbative effects at high acoustic energy densities in thermoviscous acoustofluidics, *Phys. Rev. E* **submitted**, 15 pages (2021), <https://arxiv.org/abs/2112.10737>.
- [10] R. Barnkob, P. Augustsson, T. Laurell, and H. Bruus, Acoustic radiation- and streaming-induced microparticle velocities determined by microparticle image velocimetry in an ultrasound symmetry plane, *Phys. Rev. E* **86**, 056307 (2012).
- [11] P. B. Muller, M. Rossi, A. G. Marin, R. Barnkob, P. Augustsson, T. Laurell, C. J. Kähler, and H. Bruus, Ultrasound-induced acoustophoretic motion of microparticles in three dimensions, *Phys. Rev. E* **88**, 023006 (2013).
- [12] P. B. Muller and H. Bruus, Numerical study of thermoviscous effects in ultrasound-induced acoustic streaming in microchannels, *Phys. Rev. E* **90**, 043016 (2014).
- [13] J. S. Bach and H. Bruus, Theory of pressure acoustics with viscous boundary layers and streaming in curved elastic cavities, *J. Acoust. Soc. Am.* **144**, 766 (2018).
- [14] M. A. Solovchuk, T. W. Sheu, M. Thiriet, and W.-L. Lin, On a computational study for investigating acoustic streaming and heating during focused ultrasound ablation of liver tumor, *Appl. Therm. Eng.* **56**, 62 (2013).
- [15] M. A. Solovchuk, M. Thiriet, and T. W. Sheu, Computational study of acoustic streaming and heating during acoustic hemostasis, *Appl. Therm. Eng.* **124**, 1112 (2017).
- [16] A. Sedaghatkish, M. Rezaeian, H. Heydari, A. M. Ranjbar, and M. Soltani, Acoustic streaming and thermosensitive liposomes for drug delivery into hepatocellular carcinoma tumor adjacent to major hepatic veins; an acoustics–thermal–fluid–mass transport coupling model, *Int. J. Therm. Sci.* **158**, 106540 (2020).
- [17] A. Ozcelik, D. Ahmed, Y. Xie, N. Nama, Z. Qu, A. A. Nawaz, and T. J. Huang, An acoustofluidic micromixer via bubble inception and cavitation from microchannel sidewalls, *Anal. Chem.* **86**, 5083 (2014).
- [18] M. V. Patel, I. A. Nanayakkara, M. G. Simon, and A. P. Lee, Cavity-induced microstreaming for simultaneous on-chip pumping and size-based separation of cells and particles, *Lab Chip* **14**, 3860 (2014).
- [19] H. Bachman, C. Chen, J. Rufo, S. Zhao, S. Yang, Z. Tian, N. Nama, P.-H. Huang, and T. J. Huang, An acoustofluidic device for efficient mixing over a wide range of flow rates, *Lab Chip* **20**, 1238 (2020).
- [20] C. Zhang, P. Brunet, L. Royon, and X. Guo, Mixing intensification using sound-driven micromixer with sharp edges, *Chem. Eng. J.* **410**, 128252 (2021).
- [21] M. Wiklund, R. Green, and M. Ohlin, Acoustofluidics 14: Applications of acoustic streaming in microfluidic devices, *Lab Chip* **12**, 2438 (2012).
- [22] D. J. Collins, Z. Ma, and Y. Ai, Highly localized acoustic streaming and size-selective submicrometer particle concentration using high frequency microscale focused acoustic fields, *Anal. Chem.* **88**, 5513 (2016).
- [23] D. J. Collins, Z. Ma, J. Han, and Y. Ai, Continuous micro-vortex-based nanoparticle manipulation via focused surface acoustic waves, *Lab Chip* **17**, 91 (2017).
- [24] J. D. Adams, C. L. Ebbesen, R. Barnkob, A. H. J. Yang, H. T. Soh, and H. Bruus, High-throughput, temperature-controlled microchannel acoustophoresis device made with rapid prototyping, *J Micromech Microeng* **22**, 075017 (2012).
- [25] M. Antfolk, C. Magnusson, P. Augustsson, H. Lilja, and T. Laurell, Acoustofluidic, label-free separation and simultaneous concentration of rare tumor cells from white blood cells, *Anal. Chem.* **87**, 9322 (2015).
- [26] A. Urbansky, F. Olm, S. Scheduling, T. Laurell, and A. Lenshof, Label-free separation of leukocyte subpopulations using high throughput multiplex acoustophoresis,

- [Lab Chip](#) **19**, 1406 (2019).
- [27] W. Qiu, J. T. Karlsen, H. Bruus, and P. Augustsson, Experimental characterization of acoustic streaming in gradients of density and compressibility, [Phys. Rev. Appl.](#) **11**, 024018 (2019).
- [28] R. Barnkob, C. J. Kähler, and M. Rossi, General defocusing particle tracking, [Lab Chip](#) **15**, 3556 (2015).
- [29] R. Barnkob and M. Rossi, General defocusing particle tracking: fundamentals and uncertainty assessment, [Exp. Fluids](#) **61**, 110 (2020).
- [30] M. Rossi and R. Barnkob, A fast and robust algorithm for general defocusing particle tracking, [Meas. Sci. Technol.](#) **32**, 014001 (2020).
- [31] R. Barnkob, P. Augustsson, T. Laurell, and H. Bruus, Measuring the local pressure amplitude in microchannel acoustophoresis, [Lab Chip](#) **10**, 563 (2010).
- [32] P. Augustsson, R. Barnkob, S. T. Wereley, H. Bruus, and T. Laurell, Automated and temperature-controlled micro-PIV measurements enabling long-term-stable microchannel acoustophoresis characterization, [Lab Chip](#) **11**, 4152 (2011).
- [33] R. Barnkob, I. Iranmanesh, M. Wiklund, and H. Bruus, Measuring acoustic energy density in microchannel acoustophoresis using a simple and rapid light-intensity method, [Lab Chip](#) **12**, 2337 (2012).